J. Fluid Mech. (2012), *vol.* 707, *pp.* 129–149.
doi:10.1017/jfm.2012.267

Flexible ring flapping in a uniform flow

Boyoung Kim[1], Wei-Xi Huang[2], Soo Jai Shin[1] and Hyung Jin Sung[1]†

[1] Department of Mechanical Engineering, KAIST, 291 Daehak-ro, Yuseong-gu, Daejeon 305-701, Korea
[2] Department of Engineering Mechanics, Tsinghua University, Beijing 100084, China

(Received 12 July 2011; revised 21 May 2012; accepted 2 June 2012;
first published online 2 August 2012)

An improved version of the immersed boundary (IB) method for simulating an initially circular or elliptic flexible ring pinned at one point in a uniform flow has been developed. The boundary of the ring consists of a flexible filament with tension and bending stiffness. A penalty method derived from fluid compressibility was used to ensure the conservation of the internal volume of the flexible ring. At $Re = 100$, two different flapping modes were identified by varying the tension coefficient for a fixed bending stiffness, or by changing the bending coefficient for a fixed tension coefficient. The optimal tension and bending coefficients that minimize the drag force of the flexible ring were found. Visualization of the vorticity field showed that the two flapping modes correspond to different vortex shedding patterns. We observed the hysteresis property of the flexible ring, which exhibits bistable states over a range of flow velocities depending on the initial inclination angle, i.e. one is a stationary stable state and the other a self-sustained periodically flapping state. The Reynolds number range of the bistability region and the flapping amplitude were determined for various aspect ratios a/b. For $a/b = 0.5$, the hysteresis region arises at the highest Reynolds number and the flapping amplitude in the self-sustained flapping state is minimized. A new bistability phenomenon was observed: for certain aspect ratios, two periodically flapping states coexist with different amplitudes in a particular Reynolds number range, instead of the presence of a stationary stable state and a periodically flapping state.

Key words: drag reduction, flow-structure interactions, swimming/flying

1. Introduction

Systems involving flexible bodies interacting with a surrounding fluid flow are commonplace, e.g. flying birds, swimming fish and flapping flags on the macro-scale and cells swimming in blood on the micro-scale. The mechanics of elastic bodies immersed in a viscous flow has been studied by many researchers in biology, bioengineering and chemical engineering. Analysing fluid–structure interactions helps us to understand how fish, birds and cells move in fluids such as water, air and blood. More importantly, these results have potential applications in biomimetic engineering, bioengineering and industrial engineering.

In their study of a typical fluid–flexible body interaction problem, Zhang *et al.* (2000) visualized the motion of flexible filaments in a flowing soap film by using a two-dimensional flag-in-the-wind model. They found two distinct stable states for a

† Email address for correspondence: hjsung@kaist.ac.kr

single filament that depend only on the initial inclination angle: the stretched-straight state and the self-sustained flapping state. This study inspired several numerical simulations of the interactions between flexible filaments and viscous fluid flows (e.g. Zhu & Peskin 2002; Farnell, David & Barton 2004; Yu 2005; Huang, Shin & Sung 2007). However, in contrast to the assumptions of these studies, there is usually some fluid volume inside the thin skins of organisms. For instance, the interior of a fish mostly consists of water, as is widely known. Cells consist of cell membranes and protoplasm; protoplasm is mostly fluid cell sap. Thus, to understand the motions of living bodies and cells, previous models for fluid–flexible body interactions need to be extended. To simplify these systems, we can treat them as consisting of a flexible ring filled with fluid in a fluid flow. Unlike the flapping of a filament in a viscous flow, flexible rings interacting with a surrounding fluid flow have been subjected to only a few studies. Jung *et al.* (2006) carried out an experimental study on a deformable ring in a flowing soap film. They observed the bistability phenomenon of the ring by varying the initial angle of the ring and the 2-pair (2P) mode of the wake flow of the ring. In their study the fluid was free to pass over the ring so the volume of the ring was changing. Shoele & Zhu (2010) numerically studied the flow-induced vibrations of an initially circular flexible ring without bending rigidity at a much lower Reynolds number. They identified the transverse pitching–flexible bending motion and the longitudinal tapping motion by using mode decomposition. By varying the tension coefficient, they found resonance between the fluid and the ring and observed abrupt jumps in the hydrodynamic loads. However, vortex shedding patterns undergoing resonance remain similar to those of a highly flexible ring and a nearly rigid ring. Only 2-single (2S) modes were displayed, unlike the experimental observations of Jung *et al.* (2006). They attributed such a difference to the low Reynolds number considered in the simulation.

Despite Shoele & Zhu's (2010) work on the flexible ring flapping in fluid flow, several aspects remain unclear. First, the different flapping behaviours have not been related to the vortex shedding patterns. Second, the effect of the bending rigidity and the initial reference shape of the ring have not been taken into account. Third, the hysteresis or the bistability property of the flexible ring observed in the experiment of Jung *et al.* (2006) has not been investigated numerically. To clarify the above issues, we simulated the flapping motions of a flexible ring containing fluid in a uniform flow. To this end, we made a small change to the traditional immersed boundary (IB) method by combining it with the penalty method for volume conservation, which uses proportional control and integral control derived from the fluid compressibility. In the formulation of the ring motion, we included the bending force, which enables us to simulate an initially elliptic ring rather than a circular one. The flapping phenomena and vortical structures of the flexible ring in a uniform flow were investigated numerically in the Reynolds number range $5 \leqslant Re \leqslant 120$. We determined the variations of the flapping amplitude, drag coefficient, lift coefficient, Strouhal number and vortical structures of the flexible ring with the tension coefficient (k), the bending coefficient (γ) and the aspect ratio (a/b). The hysteresis property of the flexible ring was also observed and analysed. In the next section, we introduce the problem formulation and numerical method, and the penalty method for volume conservation is derived. Then in § 3, we present the numerical results, with particular focus on the flapping modes and the hysteresis property of the flexible ring. Finally, conclusions are drawn in § 4.

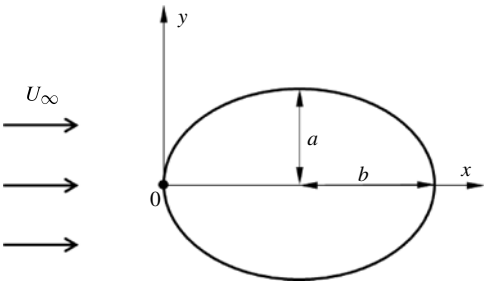

FIGURE 1. Schematic of an initially elliptic flexible ring in a uniform flow.

2. Computational model

2.1. *Problem formulation*

A schematic diagram of the computational model and the coordinate system is shown in figure 1. An initially elliptic flexible ring with one point pinned in space is subjected to a uniform incoming flow. The fluid motion is defined in Eulerian coordinates, and the origin is located at the pinned point of the ring. The incompressible viscous flow is governed by the Navier–Stokes (NS) equation and the continuity equation,

$$\rho_0 \left(\frac{\partial \boldsymbol{u}}{\partial t} + \boldsymbol{u} \cdot \nabla \boldsymbol{u} \right) = -\nabla p + \mu \nabla^2 \boldsymbol{u} + \boldsymbol{f}, \tag{2.1}$$

$$\nabla \cdot \boldsymbol{u} = 0, \tag{2.2}$$

where $\boldsymbol{u}$ is the velocity vector, p is the pressure, ρ_0 is the fluid density, μ is the dynamic viscosity of the fluid, and $\boldsymbol{f}$ is the Eulerian momentum force acting on the surrounding fluid due to the immersed boundary, as constrained by the no-slip boundary condition.

The motion of the flexible ring is described with Lagrangian variables and can be expressed as

$$\rho_1 \frac{\partial^2 \boldsymbol{X}}{\partial t^2} = \frac{\partial}{\partial s} \left(k \left(\left| \frac{\partial \boldsymbol{X}}{\partial s} \right| - 1 \right) \frac{\partial \boldsymbol{X}}{\partial s} \Big/ \left| \frac{\partial \boldsymbol{X}}{\partial s} \right| \right) - \frac{\partial^2}{\partial s^2} \left(\gamma (\kappa - \kappa_0) \frac{\partial^2 \boldsymbol{X}}{\partial s^2} \Big/ \left| \frac{\partial^2 \boldsymbol{X}}{\partial s^2} \right| \right) - \boldsymbol{F}, \tag{2.3}$$

where s is the Lagrangian coordinate along the ring, $\boldsymbol{X} = (X(s,t), Y(s,t))$ is the position, k is the tension coefficient of the ring, γ is the bending coefficient, $\kappa = \left| \partial^2 \boldsymbol{X} / \partial s^2 \right|$ is the curvature with κ_0 its initial reference value, and ρ_1 denotes the additional boundary density. The last term $-\boldsymbol{F}$ represents the Lagrangian momentum force acting on the ring due to the surrounding fluid. According to (2.3), the stressless reference state of the ring is set to be its initial undeformed shape in the present study. We would like to point out that in Shoele & Zhu (2010), the reference state for tension is the zero-length state, i.e. $T = k\,|\partial \boldsymbol{X} / \partial s|$. Thus the ring is always prestressed initially using Shoele and Zhu's formulation and is much stiffer than ours for the same k, which may cause a serious difference in the results when coupling with the fluid, as can be seen in the next section. Moreover, the boundary condition at the pinned point is given by

$$\boldsymbol{X} = (0, 0)\,, \quad \frac{\partial^2 \boldsymbol{X}}{\partial s^2} = (0, 0)\,. \tag{2.4}$$

We selected the fluid density ρ_0, the ring diameter D in the case of a circular ring or the equivalent diameter of an elliptic ring, and the uniform incoming flow velocity U_∞ as the characteristic density, length and velocity, respectively. Thus we introduced the following characteristic scales: D/U_∞ for the time, $\rho_0 D$ for the boundary mass, $\rho_0 U_\infty^2$ for the pressure and the Lagrangian momentum force $\boldsymbol{F}$, $\rho_0 U_\infty^2/D$ for the Eulerian momentum force $\boldsymbol{f}$, $\rho_0 U_\infty^2 D$ for the tension coefficient k, and $\rho_0 U_\infty^2 D^3$ for the bending coefficient γ. For convenience, in the remainder of this paper the dimensionless quantities are written in the same form as their dimensional counterparts. After non-dimensionalization, (2.1) and (2.3) take the following dimensionless forms:

$$\frac{\partial \boldsymbol{u}}{\partial t} + \boldsymbol{u}\cdot\nabla\boldsymbol{u} = -\nabla p + \frac{1}{Re}\nabla^2\boldsymbol{u} + \boldsymbol{f}, \tag{2.5}$$

$$\rho\frac{\partial^2 \boldsymbol{X}}{\partial t^2} = \frac{\partial}{\partial s}\left(k\left(\left|\frac{\partial \boldsymbol{X}}{\partial s}\right| - 1\right)\frac{\partial \boldsymbol{X}}{\partial s}\Big/\left|\frac{\partial \boldsymbol{X}}{\partial s}\right|\right) - \frac{\partial^2}{\partial s^2}\left(\gamma(\kappa-\kappa_0)\frac{\partial^2 \boldsymbol{X}}{\partial s^2}\Big/\left|\frac{\partial^2 \boldsymbol{X}}{\partial s^2}\right|\right) - \boldsymbol{F}, \tag{2.6}$$

with $Re = \rho_0 U_\infty D/\mu$ and $\rho = \rho_1/\rho_0 D$, while the continuity equation (2.2) keeps its original form.

Coupling of the fluid and the ring is formulated according to the IB method in terms of the momentum forces $\boldsymbol{F}$ and $\boldsymbol{f}$. The Lagrangian force $\boldsymbol{F}$ can be calculated along the IB by using the feedback law (Goldstein, Handler & Sirovich 1993)

$$\boldsymbol{F} = \alpha\int_0^t (\boldsymbol{U}_{ib} - \boldsymbol{U})\,\mathrm{d}t + \beta(\boldsymbol{U}_{ib} - \boldsymbol{U}), \tag{2.7}$$

where α and β are large negative free constants, $\boldsymbol{U}_{ib}$ is the fluid velocity calculated by interpolation at the IB, and $\boldsymbol{U}$ is the velocity of the ring given by $\boldsymbol{U} = \partial \boldsymbol{X}/\partial t$, with $\boldsymbol{X}$ as determined by (2.6). The Lagrangian and Eulerian variables were transformed by using the smoothed approximation of the Dirac delta function δ. In detail, the fluid velocity is interpolated at the immersed boundary, as expressed by

$$\boldsymbol{U}_{ib}(s,t) = \int_\Omega \boldsymbol{u}(x,t)\delta(\boldsymbol{X}(s,t) - x)\,\mathrm{d}x. \tag{2.8}$$

Here, we use the four-point smoothed delta function introduced by Peskin (2002). Meanwhile, the Lagrangian force is spread to the nearby Eulerian grids by using the following expression:

$$f(x,t) = \int_\Gamma \boldsymbol{F}(s,t)\delta(\boldsymbol{x} - \boldsymbol{X}(s,t))\,\mathrm{d}s. \tag{2.9}$$

Note that the smoothed delta function is two-dimensional for both the velocity interpolation (2.8) and the force spread (2.9), while the integral is two-dimensional for the former but only one-dimensional for the latter. Thus the Eulerian momentum force $\boldsymbol{f}$ is singular and might cause a pressure jump in the fluid across the ring. In the simulation, $\boldsymbol{f}$ is actually distributed over several Eulerian grids in width by using the smoothed delta function.

2.2. *Volume conservation*

Since the fluid inside the ring is incompressible and enclosed by the ring, the internal volume of the flexible ring is expected to be conserved. However, the problem of volume leakage arises when the traditional IB method is used for solving fluid–flexible body interactions because of its use of the smoothed approximation to the Dirac delta

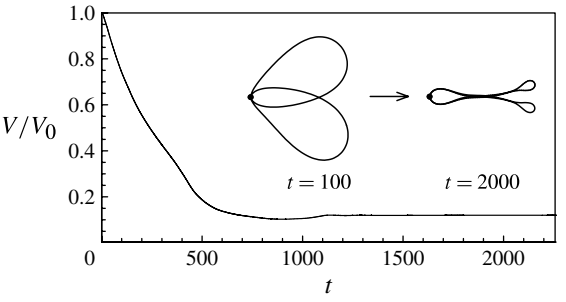

FIGURE 2. Changes in the interior volume of a flexible ring with $k = 10$ and $\gamma = 0.01$ in a uniform flow without volume conservation.

function. Figure 2 shows the evolution of the volume of a flexible ring in a uniform flow and the instantaneous shapes without any treatment for volume conservation. A tension coefficient of $k = 10$ and a bending coefficient of $\gamma = 0.01$ were used in this case. From figure 2 we can see that the volume of the ring converges at 18 % of its initial value, which means that 82 % of the initial volume penetrates from the inside of the flexible ring to the outside. The instantaneous shape in figure 2 at $t = 2000$ shows a severe volume leakage when the vibration of the ring is stabilized, which makes the result unacceptable.

Several methods for volume conservation have been proposed by using the projection approach or incorporating the jump conditions in stress at the interface, which require more complicated implementations and computational time (Cortez & Minion 2000; Li & Lai 2001; Peskin & Printz 2002). Recently, Peng, Asaro & Zhu (2010) proposed a penalty method derived from fluid compressibility that aims to improve the conservation of cell volume during deformation. Here we adopt a similar approach to that of Peng *et al.* due to its simplicity in implementation.

The fluid compressibility β is defined as

$$\beta = -\frac{1}{V}\frac{\partial V}{\partial p}, \tag{2.10}$$

where V denotes the fluid volume inside the ring in the present study and p denotes the pressure. The pressure gradient can be expressed as

$$\partial p = -\frac{1}{\beta}\frac{\partial V}{V}. \tag{2.11}$$

Then integrating (2.11) yields

$$\int \partial p = -\frac{1}{\beta}\int \frac{1}{V}\partial V, \tag{2.12}$$

$$\Delta p = -\frac{1}{\beta}\ln\left(\frac{V}{V_0}\right), \tag{2.13}$$

where Δp denotes the pressure difference between the interior and exterior of the ring, and V_0 denotes the initial interior volume of the ring. By assuming a small change in

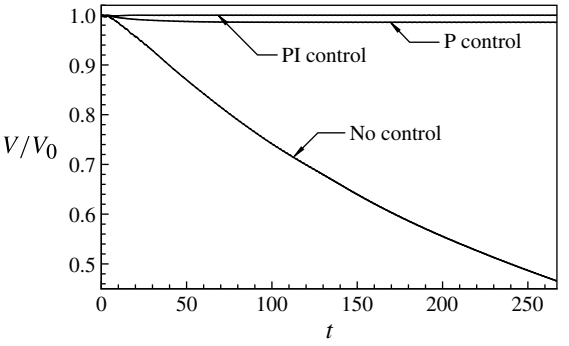

FIGURE 3. Changes in the volume of the flexible ring with no control, P control, and PI control.

volume V from V_0, (2.13) can be approximated by

$$\Delta p = \frac{1}{\beta}\left(1 - \frac{V}{V_0} + \frac{1}{2}\left(1 - \frac{V}{V_0}\right)^2 + \cdots\right) \approx \frac{1}{\beta}\left(1 - \frac{V}{V_0}\right), \tag{2.14}$$

using Taylor's expansion. Moreover, to represent historical effects, we can also add an integral term to (2.14), which becomes

$$\Delta p = \frac{1}{\beta}\left(1 - \frac{V}{V_0}\right) + \frac{1}{\beta}\int_0^t \left(1 - \frac{V}{V_0}\right) \mathrm{d}t', \tag{2.15}$$

where t is the present time. The pressure difference Δp computed from (2.15) is then used to calculate the penalty force for volume conservation,

$$\boldsymbol{F}_A(s) = \Delta p \boldsymbol{e}_n, \tag{2.16}$$

where $\boldsymbol{e}_n$ denotes the local normal unit in the direction from the interior to the exterior of the ring. This calculated penalty force is then added to the structure motion equation as an external force term, i.e.

$$\rho\frac{\partial^2 \boldsymbol{X}}{\partial t^2} = \frac{\partial}{\partial s}\left(k\left(\left|\frac{\partial \boldsymbol{X}}{\partial s}\right| - 1\right)\frac{\partial \boldsymbol{X}}{\partial s}\Big/\left|\frac{\partial \boldsymbol{X}}{\partial s}\right|\right) - \frac{\partial^2}{\partial s^2}\left(\gamma(\kappa - \kappa_0)\frac{\partial^2 \boldsymbol{X}}{\partial s^2}\Big/\left|\frac{\partial^2 \boldsymbol{X}}{\partial s^2}\right|\right) - \boldsymbol{F} + \boldsymbol{F}_A. \tag{2.17}$$

Figure 3 shows the time histories of the changes in volume with and without the penalty method for volume conservation, where 'P control' denotes the result obtained with the penalty method using (2.14) and 'PI control' denotes that obtained using (2.15). As shown in figure 3, the P control and PI control results show significantly improved volume conservation. For P control, a small volume leakage is still observed during the initial stage, which can be corrected by taking into account the historical effect, i.e. the PI control. Hence we adopt PI control in the following simulations.

2.3. *Numerical method and validation*

The numerical description of the fluid–ring interaction system has three components, i.e. the fluid solution, the solid solution, and the coupling scheme. For the fluid motion, the NS equations are solved with the fractional step method on a staggered Cartesian

	h	Δt	C_D	$C_{l,rms}$	St
Case 1	1/32	2.0×10^{-3}	1.55	0.28	0.177
Case 2	1/64	2.0×10^{-3}	1.53	0.28	0.178
Shin *et al.*	1/64	6.0×10^{-3}	1.44	0.35	0.168
Lai and Peskin	1/64	1.8×10^{-3}	1.52	0.29	0.155
Lai and Peskin	1/128	9.0×10^{-4}	1.45	0.33	0.165
Uhlmann	1/128	3.0×10^{-3}	1.50	0.35	0.172

TABLE 1. Drag and lift coefficients and the Strouhal number of a rigid cylinder in a uniform flow at $Re = 100$.

grid (Kim, Baek & Sung 2002). Fully implicit time advancement is employed; the Crank–Nicolson scheme is used for the discretization of the diffusion and convection terms. The decoupling of the velocity and pressure is achieved by using block LU decomposition in conjunction with approximate factorization. The ring motion is defined in the Lagrangian coordinates on a staggered grid system, with the tension force defined on the interfaces and the other variables defined on the nodes. The motion equation of the ring is discretized in space by using the finite difference method and is advanced in time by using a semi-implicit scheme in which the tension force term is treated implicitly and the bending force term is treated explicitly. The fluid and solid solvers are then coupled by using the IB method in an explicit way, without iteration at each time step. The details of the numerical method can be found in Huang *et al.* (2007).

First, we simulated flow over a rigid circular cylinder. In this case, the momentum force $\boldsymbol{F}$ was calculated with (2.7) by specifying $\boldsymbol{U} = 0$. The Reynolds number was set at 100, based on the uniform flow velocity and the cylinder diameter (D). The fluid domain size was $L_x/D = 32$ and $L_y/D = 16$ in the x and y directions, respectively, with the corresponding grid numbers $N_x = 1024$ and $N_y = 512$. The number of Lagrangian points along the cylinder surface was 128. A comparison of the present results with data from other numerical studies and experiments is provided in table 1, including the root mean squares (r.m.s.) of the lift coefficient $C_{l,rms}$, the mean drag coefficient C_D, and the Strouhal number; good agreement is evident.

Next we considered the free vibration of a flexible ring immersed in an ambient quiescent fluid. The initial shape of the ring was set at $r(\theta, 0) = R(1 + \varepsilon \cos q\theta)$, where R is the radius in the equilibrium state, q is an integer representing the wavenumber around the ring, and $\varepsilon \ll 1$. In this simulation, the fluid domain size is 8.0×8.0, scaled by the ring diameter $2R$, with a grid number of 256×256, and the number of Lagrangian points along the ring is also 128. The ring is released when the simulation starts and undergoes a standing-wave vibration with the prescribed wavenumber q. To compare with the result of Shoele & Zhu (2010), in the simulation we used the same formulation of the tension force as theirs, i.e. $T = k\partial \boldsymbol{X}/\partial s$, and set the same dimensionless tension coefficient, i.e. $kR/\rho_0\nu^2 = 2.51 \times 10^5$. Figure 4 shows the time history of the radial position of a point $r(\theta, t)$ on the ring with $\theta = \pi$, and we can find excellent agreement with the result of Shoele & Zhu (2010). Moreover, by fitting the curve in figure 4 to the form $R(1 + \varepsilon e^{\alpha t} \cos \beta t \cos q\theta)$ using the method of least squares, we obtained the decay rate α and the frequency β, i.e. $\alpha R^2/\nu = -46.5$ and $\beta R^2/\nu = 1029.4$, which also coincide with the numerical result of Shoele & Zhu (2010) as well as the analytical solution of Cortez *et al.* (2004).

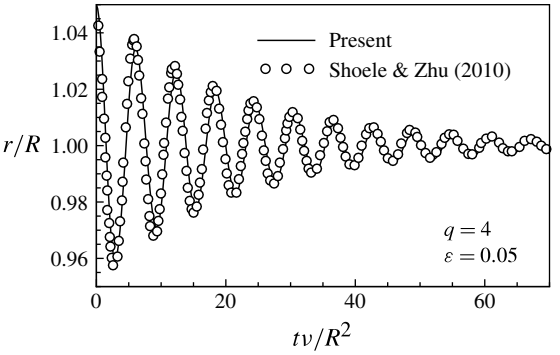

FIGURE 4. The radial position of a point on the ring at $\theta = \pi$ with initial disturbance $r(\theta, t = 0) = R(1 + \varepsilon \cos q\theta)$ in a quiescent fluid, together with the result of previous research (Shoele & Zhu 2010) with $q = 4$, $\varepsilon = 0.05$ and $kR/\rho_0\nu^2 = 2.51 \times 10^5$.

3. Results and discussion

3.1. *Flapping modes*

In this section we first consider an initially circular flexible ring, i.e. $R = a = b$ (figure 1). The ring with one point pinned in space that is set as the origin of the coordinates is subjected to a uniform flow. The computational parameters, including the Reynolds number, the domain size and the corresponding grid number, are the same as those for the simulation of flow over a circular cylinder presented in the previous section, except that the number of Lagrangian points along the ring is increased to 256. The flapping phenomena and the wake flow of the ring were examined by varying the tension coefficient (k), the bending coefficient (γ) and the aspect ratio (a/b). In our simulations, the tension coefficient k ranges from 6 to 400, while the bending coefficient γ ranges from 0 to 0.25.

3.1.1. *Identification of flapping modes*

Figure 5 shows the mean drag coefficient (C_D) of the flexible ring as a function of the tension coefficient for various bending coefficients. It is clearly seen that most curves can be divided into two regions: the drag coefficient decreases at first as k increases since the ring becomes stiffer and more resistive to deformation, and then abruptly jumps to a high value at a critical k. The jump of C_D as k increases has also been reported by Shoele & Zhu (2010), where a relatively narrow peak of C_D was observed, and they attributed it to the fluid–structure resonance. Here we refer to this phenomenon as the mode transition, since C_D stays relatively stable above the critical k in our simulations, and more evidence is presented later. Superposition of the instantaneous ring shapes of four selected cases, i.e. $k = 7$, 10 and 11 with $\gamma = 0.01$ and $k = 10$ with $\gamma = 0$, is shown in figure 6. We can see the obvious difference between the two modes before and after the jump of C_D as k increases, e.g. $k = 10$ and 11 for $\gamma = 0.01$ (figure 6*b*,*c*), which are termed the 'ordinary mode' and the 'energetic mode' respectively in the present study. Moreover, from figure 6(*a*,*d*) it is shown that a decrease of k or γ also induces significant changes in the span of flapping as compared with the ordinary mode, which will be discussed later.

To study the two flapping modes in more detail, the time histories of the drag coefficient (C_d), the lift coefficient (C_l) as well as the transverse position of the mid-point of the ring (y_m) are plotted in figure 7 for the four cases corresponding

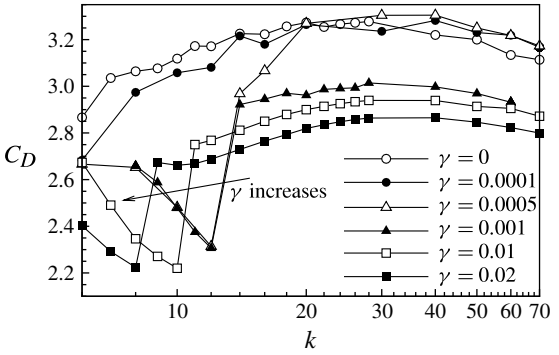

FIGURE 5. Variation of the mean drag coefficient of a flexible ring as a function of the tension coefficient for various bending coefficients.

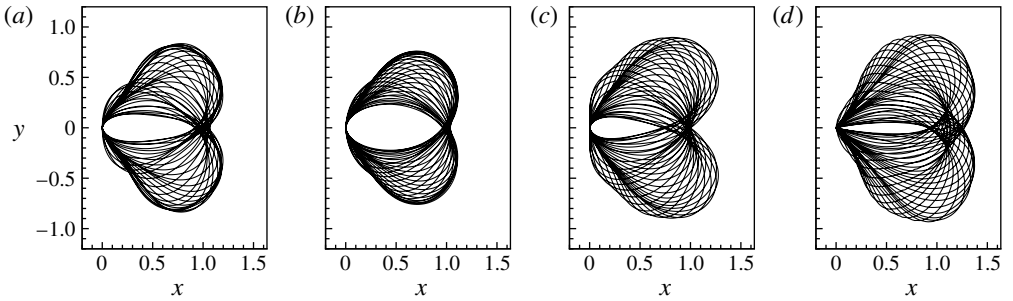

FIGURE 6. Instantaneous shapes of a flexible ring with: (*a*) $k = 7$, $\gamma = 0.01$; (*b*) $k = 10$, $\gamma = 0.01$; (*c*) $k = 11$, $\gamma = 0.01$; and (*d*) $k = 10$, $\gamma = 0$.

to figure 6. By comparing the two cases of $k = 10$ and 11 for $\gamma = 0.01$, as the representatives of the ordinary and energetic modes respectively, it is surprisingly seen that the oscillation amplitudes of the drag and lift coefficients are much augmented for the energetic mode (figure 7*b*,*c*), more significantly than the increases in the flapping amplitude and the mean drag coefficient (figure 5). A quantitative comparison is listed in table 2. Notably, no beating behaviours of C_d and C_l are seen during the mode transition (figure 7), unlike Shoele & Zhu's (2010) results, indicating that fluid–structure resonance does not occur in the present system. Furthermore, the frequency spectra of C_l obtained by Fourier transform for the above-mentioned four cases are plotted in figure 8, where we can see that the frequency of the first harmonic (f_1) corresponds to the flapping period and the second one (f_2) corresponds to the oscillation in C_l caused by elastic vibration of the ring. It is interesting to note that the second harmonic is dominant for the ordinary mode of flapping (figure 8*b*), while the first harmonic is dominant for the energetic mode (figure 8*c*). As a result, there is an obvious difference in the phase relation between C_l and y_m for the two flapping modes, as can be seen in figure 7(*b*,*c*). Figure 9 shows the variation of the phase difference $\Delta\phi$ between the maximum C_l and the maximum y_m with k for various γ. We can see a jump of $\Delta\phi$ due to mode transition, which is $\sim 0.6\pi$ for the ordinary mode and -0.1π for the energetic mode.

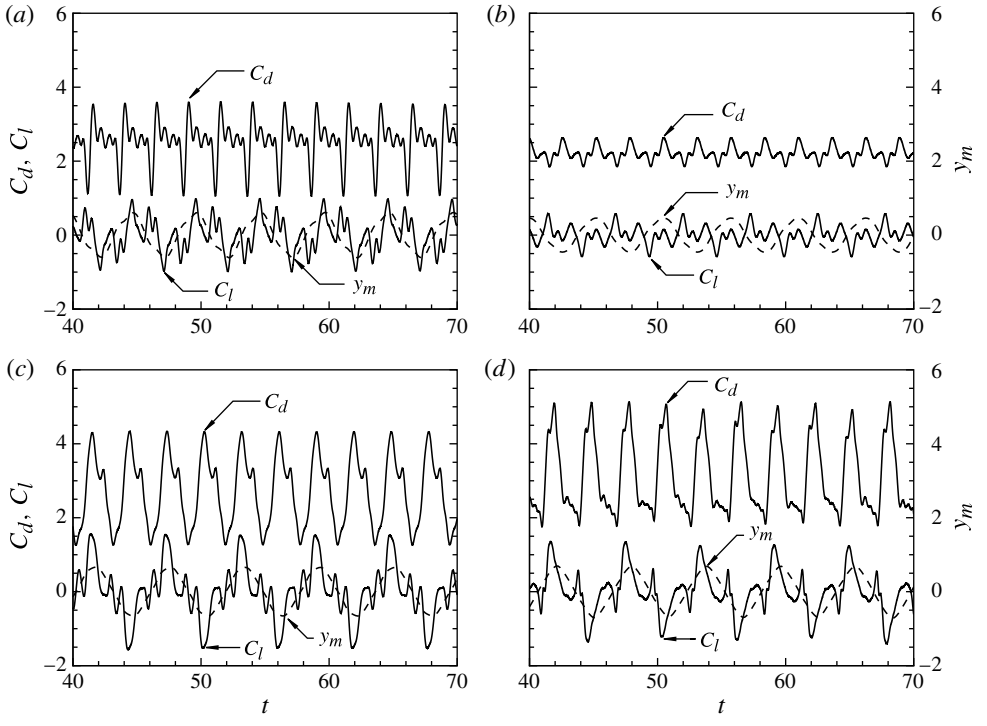

FIGURE 7. Time histories of the drag and lift coefficients and the transverse position of the mid-point of the ring for $Re = 100$: (*a*) $k = 7$, $\gamma = 0.01$; (*b*) $k = 10$, $\gamma = 0.01$; (*c*) $k = 11$, $\gamma = 0.01$; and (*d*) $k = 10$, $\gamma = 0$.

k	7	10	11	10
γ	0.01	0.01	0.01	0.0
C_D	2.4906	2.2201	2.7513	3.1186
$C_{d,rms}$	0.5072	0.1920	0.9455	0.9330
$C_{l,rms}$	0.4274	0.2391	0.7314	0.5736
St	0.1977	0.1901	0.1713	0.1707

TABLE 2. Drag and lift coefficients and the Strouhal number of a flexible ring in a uniform flow with different k and γ at $Re = 100$.

As further evidence for the explanation of such differences between the two flapping modes, the vorticity contours together with the ring shapes at the instants when the lift coefficient reaches its two positive peaks are plotted in figure 10, with those corresponding to the negative peaks omitted for the reason of symmetry. The two peaks are denoted by A and B, respectively, as shown in the left column of figure 10. For the ordinary mode (figure 10*b*), two single counter-rotating vortices are shed alternately from the flapping ring during each period, which is classified as the 2S mode (Williamson & Roshko 1988). Different from the classical cylinder wake, however, the flexible ring causes more complicated dynamics. In figure 10(*b*), instant A denotes the maximum C_l but a small negative y_m, while instant B denotes

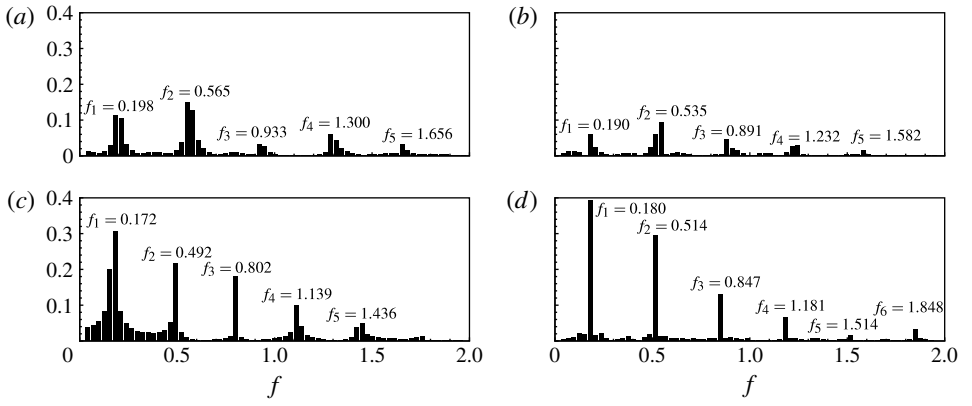

FIGURE 8. Frequency spectra of the lift coefficient of the flapping ring for $Re = 100$: (*a*) $k = 7$, $\gamma = 0.01$; (*b*) $k = 10$, $\gamma = 0.01$; (*c*) $k = 11$, $\gamma = 0.01$; and (*d*) $k = 10$, $\gamma = 0$.

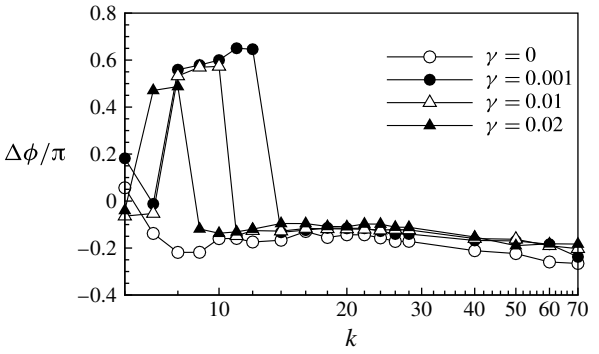

FIGURE 9. Variation of the phase difference between the maximum lift coefficient and the maximum transverse position of the mid-point of the ring as a function of the tension coefficient for various bending coefficients.

the second maximum C_l near the negative peak of y_m. The vorticity contours show that a positive vortex is shed from the lower side of the ring at instant B due to the transverse flapping motion, resulting in a local maximum C_l, while at instant A the vortex is still attached and growing at the lower side of the ring, indicating that the maximum C_l is attributed to elastic vibration of the ring by recalling the dominant harmonic shown in figure 8. For the energetic mode (figure 10*c*), a pair of counter-rotating vortices at instant A are shed from the leading and trailing edges, respectively, although one is dominant while the other is weak and elongated, which is not entirely separated and dissipated fast downstream. Thus we did not see the 2P mode of vortices far downstream due to the low Reynolds number in the present simulations, but near the ring the vortex pattern is 2P-like (Williamson & Roshko 1988). We see that it is the 2P-like pattern of vortex shedding that causes significant increases of C_d and C_l as compared with the ordinary mode (figure 7*b*,*c*). At instant B of the energetic mode (figure 10*c*), the local maximum of C_l is induced by elastic deformation of the ring by noting that the instantaneous vorticity field is similar to that of the ordinary mode at instant A (figure 10*b*).

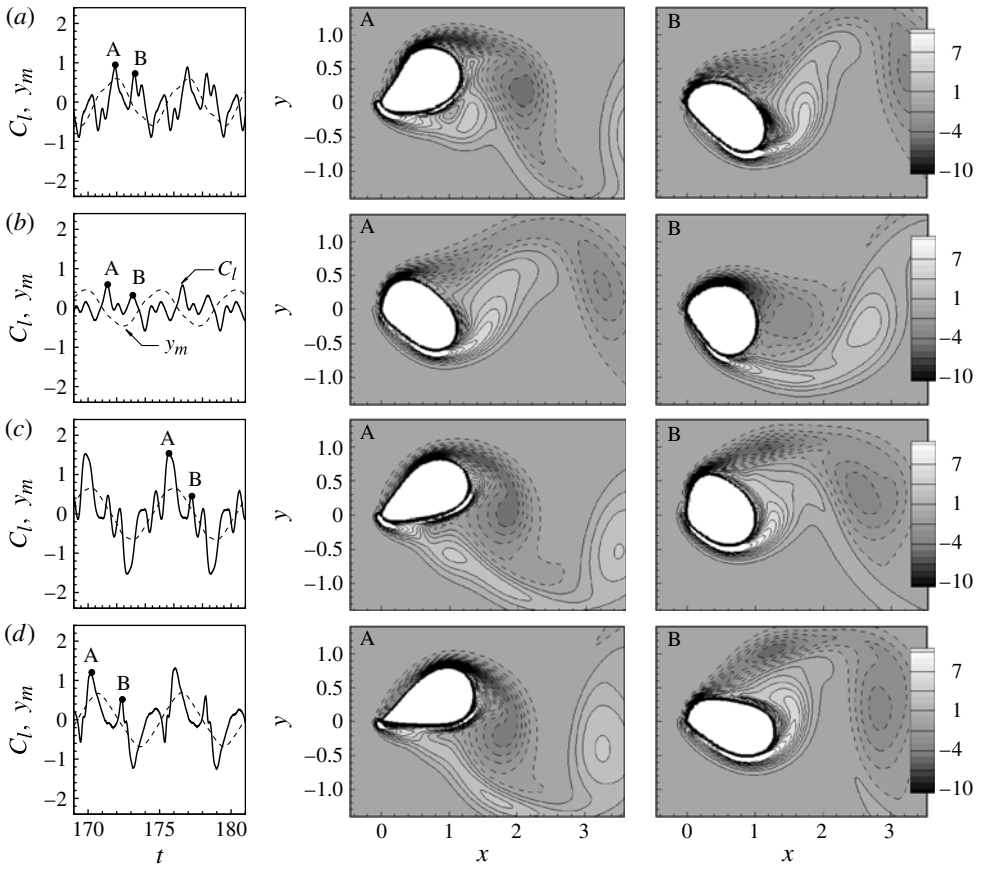

FIGURE 10. Instantaneous vorticity contours over the flapping ring at the instants when the lift coefficient reaches its two positive peaks labelled A and B for $Re = 100$: (*a*) $k = 7$, $\gamma = 0.01$; (*b*) $k = 10$, $\gamma = 0.01$; (*c*) $k = 11$, $\gamma = 0.01$; and (*d*) $k = 10$, $\gamma = 0$.

Figure 11(*a*) shows the variation of the Strouhal number with the tension coefficient k for various bending coefficients, $\gamma = 0.001$, 0.01 and 0.02. It is interesting to see that the Strouhal number is abruptly decreased due to mode transition and remains almost constant for the energetic mode, which is close to that of the wake flow over a rigid circular cylinder, i.e. $St \approx 0.17$, although the values vary slightly with the bending rigidity. Figure 10(*b*) shows the variation of the amplitude of the perimeter oscillation during flapping (A_p) with the tension coefficient k. Except for a jump at the critical k, A_p varies linearly inversely to k for both the ordinary and energetic modes due to the linear constitutive law adopted for the tension force (equation (2.3)).

3.1.2. *Other effects*

Exceptions found in figure 5 are the cases with small bending coefficients, i.e. $\gamma = 0$ and 0.0001, where no jump of C_D as k increases was detected. To facilitate comparison, a case of $k = 10$ and $\gamma = 0$ is selected, with its instantaneous shapes shown in figure 6(*d*), the time histories of C_d, C_l and y_m in figure 7(*d*), the frequency spectrum of C_l in figure 8(*d*), and the vorticity contours in figure 10(*d*). Generally speaking, we can see that the flapping motion of $k = 10$ and $\gamma = 0$ is consistent

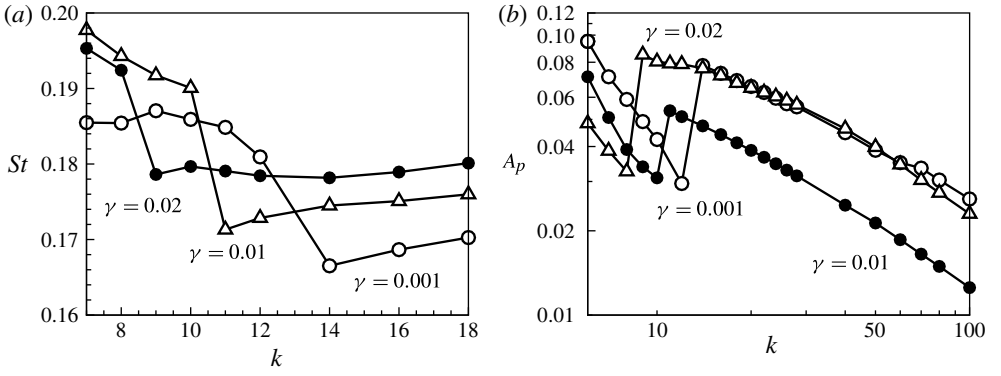

FIGURE 11. (*a*) Strouhal number and (*b*) amplitude of perimeter variation of a flexible ring as functions of the tension coefficient for various bending coefficients.

with that of $k = 11$ and $\gamma = 0.01$. Without the bending rigidity, the ring easily adapts to the streamlines of the surrounding flow and thus the transverse flapping motion is dominant over the elastic vibration, resulting in the energetic mode. Note that in Shoele & Zhu (2010) the jump of C_D was present for the ring without bending rigidity (figure 12 of their paper), since the ring is prestressed and much stiffer than ours for the same k due to the different formulation of the tension force.

Further observations on figure 5 shows that, as k decreases in the regime of the ordinary mode motion, the mean drag coefficient C_D is gradually increased to become comparable to that of the energetic mode. Further decrease in k causes some difficulties in numerical computation since the ring is elongated too much. Taking $k = 7$ and $\gamma = 0.01$ as an example, the flapping span and especially the oscillation amplitudes of the drag and lift coefficients are much increased as compared with those of the energetic mode (see figures 6*a* and 7*a*). Moreover, the phase difference $\Delta\phi$ between the maximum C_l and the maximum y_m is shifted to about zero as seen in figures 6(*a*) and 9. However, the pattern of vortex shedding remains the 2S mode (figure 10*a*), consistent with the ordinary mode. The reason for the shift in $\Delta\phi$ is the enhanced transverse flapping due to the decrease of k, which increases the vortex strength around the ring and results in the maximum C_l near the maximum y_m position. Nevertheless, the contribution to C_l is still dominant by the elastic vibration of the ring as dictated by figure 8(*a*).

Figure 12 shows the variation of the drag coefficient of the flexible ring with the bending coefficient γ for various tension coefficients, $k = 8$, 9 and 10. For each tension coefficient, as the bending coefficient increases, the drag coefficient of the flexible ring decreases at first, then abruptly increases and stays relatively stable after mode transition. This trend is similar to that of the tension effect as shown in figure 5. Hence, transition of the flapping modes can be induced by changes of not only the tension coefficient but also the bending coefficient. Combining figures 5 and 12, we see that there exists an optimal bending coefficient that minimizes the drag coefficient, which for $k = 9$ and $\gamma = 0.015$ is at $Re = 100$ in the present simulations. The instantaneous shapes of the ring corresponding to the two flapping modes by varying the bending coefficient are seen on figure 12(*b*). Similar patterns of both modes are displayed with those shown in figure 6(*b*,*c*). Moreover, variation of the phase difference $\Delta\phi$ between the maximum C_l and the maximum y_m as a function

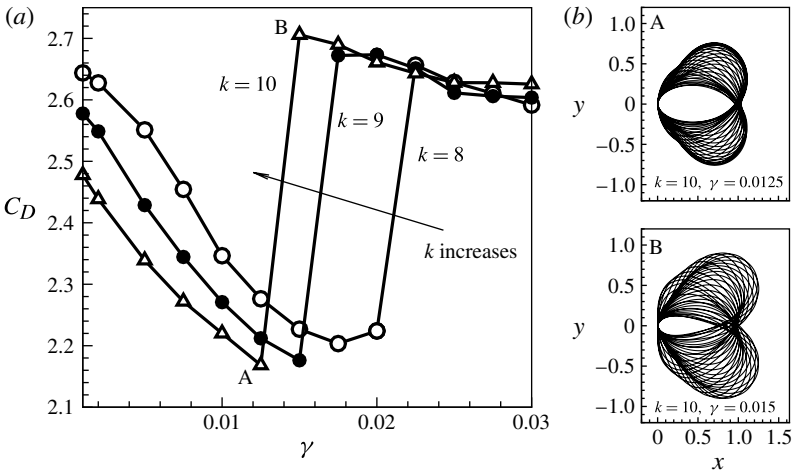

FIGURE 12. (*a*) Variation of the mean drag coefficient of a flexible ring with the bending coefficient for various tension coefficients; (*b*) instantaneous shapes of a flexible ring with $k = 10$ and different bending coefficients.

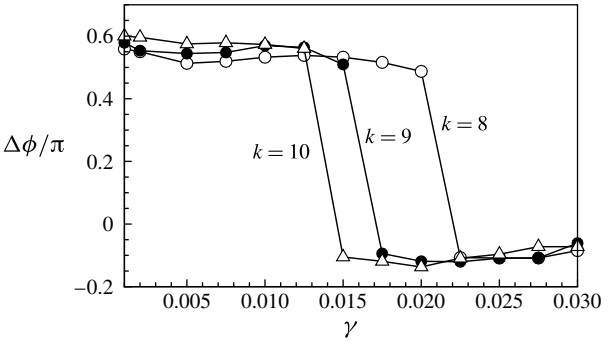

FIGURE 13. Variation of the phase difference between the maximum lift coefficient and the maximum transverse position of the mid-point of the ring as a function of the bending coefficients for various tension coefficients.

of γ is plotted in figure 13. Similar to figure 9, it is clearly shown that $\Delta\phi$ is $\sim 0.6\pi$ for the ordinary mode but is shifted to -0.1π for the energetic mode, indicating the change in the vortex shedding pattern due to mode transition.

In figure 14, the variation of the mean drag coefficient C_D with the tension coefficient is plotted for various aspect ratios (a/b, see figure 1). It is seen that the drag coefficient is decreased as a/b decreases since the ring becomes thinner, while a minimum C_D is obtained at about $a/b = 0.5$ and then is increased slightly as a/b decreases further (see the inset of figure 14) since C_D is mainly determined by the flapping amplitude for a slender ring. It is also observed that the mode transition does not occur for the cases of small aspect ratios, i.e. $a/b = 0.25$ and 0.5 in figure 14. The instantaneous shapes indicate the ordinary mode of flapping for $a/b = 0.25$ and 0.5 as shown in figure 14(*b*). On the other hand, after transition to the energetic mode for the

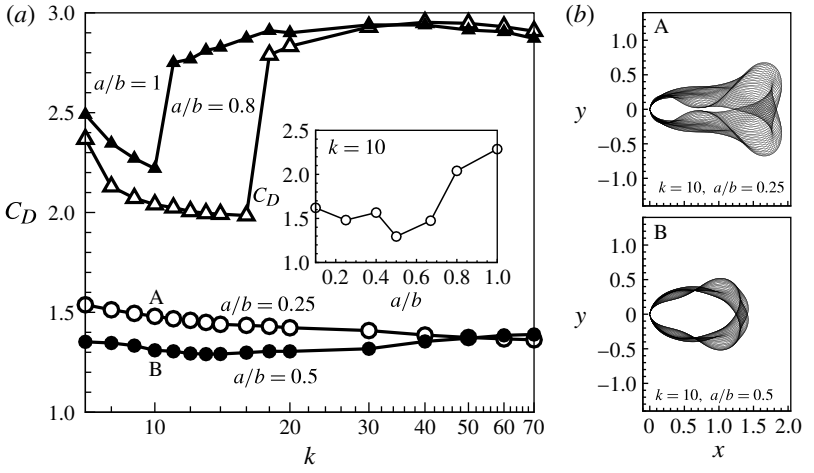

FIGURE 14. (*a*) Variation of the mean drag coefficient of a flexible ring with the tension coefficient for various aspect ratios; (*b*) instantaneous shapes of a flexible ring with $k = 10$ and different bending coefficients. Inset: variation of the mean drag force with the aspect ratio with $k = 10$.

cases of large aspect ratios, i.e. $a/b = 0.8$ and 1.0, the drag coefficient is insensitive to the aspect ratio.

3.2. *Hysteresis property*

We now reduce the Reynolds number in our simulation, and the ring will finally stop flapping and retain a stationary stable state, while in a certain range of the Reynolds number the ring exhibits hysteresis behaviour. Hysteresis behaviour of the ring in fluid flow has been observed in the experiment of Jung *et al.* (2006), but has not been reported numerically. On the other hand, extensive studies have shown hysteresis behaviour or bistability of a flexible filament or flag in fluid flow, both experimentally and numerically (Zhang *et al.* 2000; Shelley, Vandenberghe & Zhang 2005; Connell & Yue 2007; Huang *et al.* 2007; Alben & Shelley 2008; Eloy *et al.* 2008).

To scrutinize the hysteresis phenomenon of the ring, we performed simulations by varying the Reynolds number and the initial inclination angle (θ_0). Figure 15 shows the variation of the flapping amplitude with the Reynolds number for various aspect ratios, i.e. $a/b = 0.10$, 0.25, 0.40, 0.50, 0.67, 0.80 and 1.0, and for each case two initial inclination angles are compared, i.e. $\theta_0 = 0$ and $\pi/24$. For $a/b = 0.25$, the ring exhibits a stationary stable state for both $\theta_0 = 0$ and $\pi/24$ when $Re < 30$, and a periodically flapping state independent of the initial inclination angle when $Re > 50$. When the Reynolds number is between 30 and 50, a bistability region appears for which the ring is stationary and stable for $\theta_0 = 0$ but flaps periodically for $\theta_0 = \pi/24$, indicating the hysteresis behaviour. The hysteresis region arises for $a/b = 0.67$ at higher Reynolds numbers than that for $a/b = 0.25$, and the flapping amplitude is smaller. For $a/b = 1.0$ the lower limit of the hysteresis region is similar to that for $a/b = 0.25$, but the region becomes narrow. The statistics for the Reynolds number range of the hysteresis region and the flapping amplitude for various aspect ratios are plotted in figure 16. Below the hysteresis region, the ring remains stationary and stable regardless of the initial inclination angle, whereas it is always flapping above the hysteresis region. The Reynolds number at which the hysteresis region commences

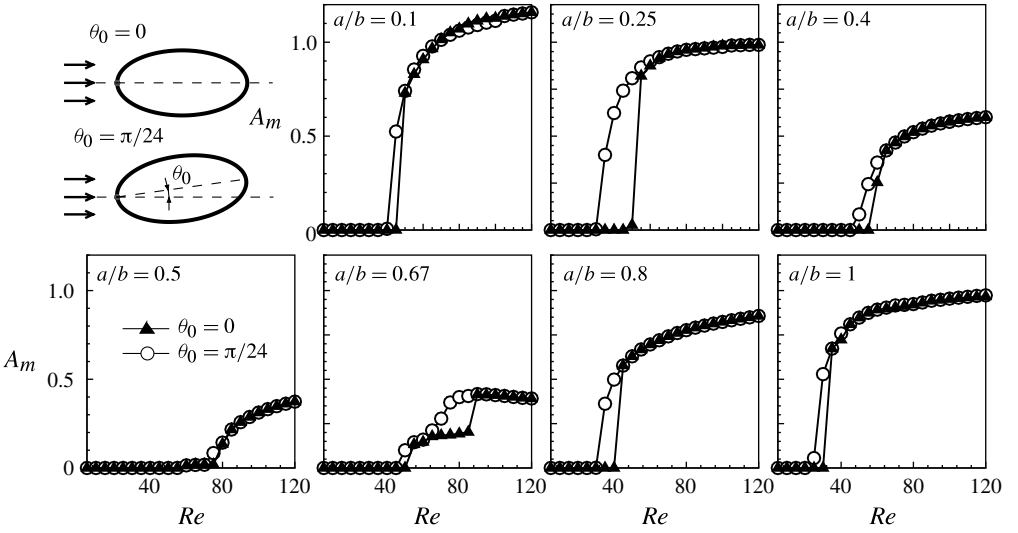

FIGURE 15. Variations of the flapping amplitude of the mid-point of a flexible ring with the Reynolds number for various aspect ratios. The shapes of the flexible ring for $a/b = 0.5$ with $\theta_0 = 0$ and $\theta_0 = \pi/24$ are depicted.

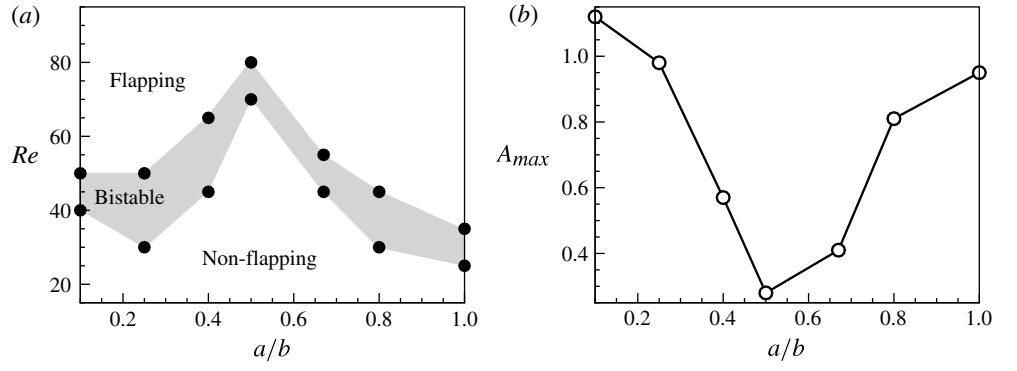

FIGURE 16. Variations of (*a*) Reynolds number range of the bistability region and (*b*) the flapping amplitude of the mid-point of the ring at $Re = 100$ as functions of the aspect ratio.

increases and then decreases as the aspect ratio increases, and reaches its maximum at about $a/b = 0.50$ (figure 16*a*). On the other hand, the flapping amplitude decreases and then increases as the aspect ratio increases, and reaches its minimum at about $a/b = 0.50$ (figure 16*b*). The results indicate that the aspect ratio of $a/b = 0.50$ is most stable to keep the stationary state of the ring, which is consistent with the result of C_D shown in figure 14.

Vorticity contours for $a/b = 0.25$ and $Re = 50$ are shown in figure 17(*a*), where we can see the bistable states of the ring. It is interesting to note that both the gliding and fluttering motions are commonly seen for flying or swimming animals, which may have some intrinsic relations with the hysteresis property displayed here. Hence, investigation on the passive flapping behaviour may help us to understand active flying

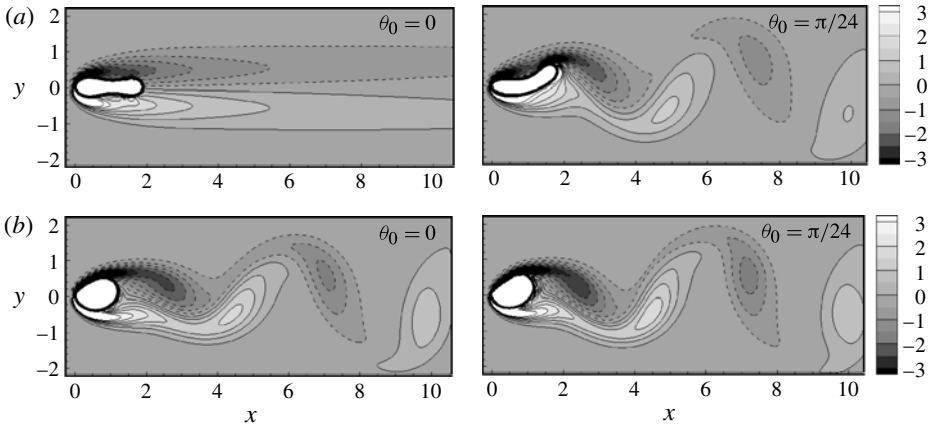

FIGURE 17. Instantaneous vorticity contours of a uniform flow over initially elliptic flexible rings for $k = 10$ and $\gamma = 0.01$: (*a*) $a/b = 0.25$, $Re = 50$; (*b*) $a/b = 0.67$, $Re = 80$.

or swimming motions in nature (Zhang *et al.* 2000; Liao *et al.* 2003; Müller 2003; Jung *et al.* 2006). An unexpected phenomenon is observed for $a/b = 0.67$ in figure 15: above the common bistability region there is another hysteresis loop within a certain range of the Reynolds number, where the ring exhibits two periodically flapping states with different amplitudes, instead of one stationary stable state and one periodically flapping state. Vorticity contours for $a/b = 0.67$ and $Re = 80$ are seen in figure 17(*b*). The present results indicate that there may exist multiple periodically flapping states of flying or swimming, which need further evidence to confirm in real life.

The hysteresis loop displayed in figure 15 is a common feature of the viscoelastic system. Here the flexible ring behaves as an elastic material and the fluid viscosity has a damping function, whereas the vortex shedding from the ring can be regarded as a periodic external force. From the stability point of view, the fluid viscosity sets a certain threshold of disturbance energy for the setting up of flapping. Thus, given a higher initial inclination angle, the critical Reynolds number is reduced, resulting in subcritical stability of the system. The hysteresis property can be described by using Landau's equation arising from nonlinear stability of viscous flow (Landau & Lifshitz 1987), i.e.

$$\frac{1}{2}\frac{\mathrm{d}A_m^2}{\mathrm{d}t} = \omega_i A_m^2 - aA_m^4 - bA_m^6, \tag{3.1}$$

where A_m denotes the flapping amplitude of the mid-point, ω_i denotes the exponential growth rate due to linear stability, while a and b are the Landau constants, which depend on the system property. The linear stability is caused by setting $a = b = 0$. The growth rate ω_i is approximately proportional to $(Re - Re_{cr})$ as Re is close to Re_{cr} because ω_i is zero for $Re = Re_{cr}$, where Re_{cr} denotes the critical Reynolds number beyond which the system is unstable for infinitesimal initial perturbation. Here we assume $a < 0$ and $b > 0$. Equation (3.1) dictates the temporal variation of the flapping amplitude A_m by setting an infinitesimal or finite-amplitude initial value, which can be rewritten as

$$\frac{1}{2}\frac{\mathrm{d}A_m^2}{\mathrm{d}t} = -bA_m^2(A_m^2 - r_1)(A_m^2 - r_2), \tag{3.2}$$

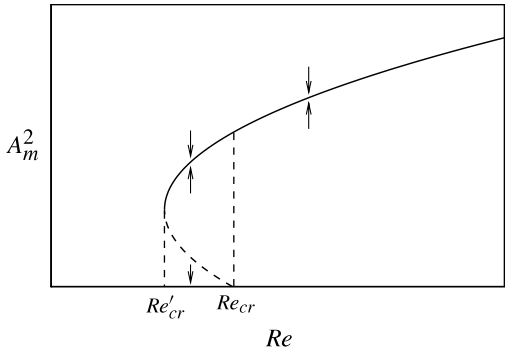

FIGURE 18. Schematic of the hysteresis property. The vertical arrays denote the convergence direction of the flapping amplitude.

where

$$r_{1,2} = -\frac{a}{2b} \pm \sqrt{\frac{a^2}{4b^2} + \frac{\omega_i}{\beta}}. \tag{3.3}$$

Equation (3.2) indicates that A_m converges to different values depending on its initial amplitude, which is shown schematically in figure 18. The upper branch (solid) and the lower branch (dashed) in figure 18 are plotted according to (3.3). For $Re > Re_{cr}$, the flapping amplitude converges to the upper branch for arbitrary initial values. However, for $Re'_{cr} < Re < Re_{cr}$, the flapping amplitude converges to the upper branch only for finite initial amplitudes above the lower branch, and decays to zero for those below the lower branch. Furthermore, to explain the hysteresis loop above the critical Reynolds number where two periodically flapping states with different amplitudes are present as seen in figure 15 for $a/b = 0.67$, a higher-order term $-cA_m^8$ needs to be put into (3.1). Using this model and following a similar analysis as above, the solution converges to two different finite amplitudes depending on its initial condition.

To further demonstrate the hysteresis property observed in $a/b = 0.67$, the phase relations between the transverse position and the transverse velocity of the mid-point of the ring at various Reynolds numbers are plotted in figure 18. At $Re = 50$, the phase trajectory remains a point at the origin for $\theta_0 = 0$ but converges to a circle for $\theta_0 = \pi/24$, whose radius denotes the flapping amplitude. At $Re = 70$, the phase trajectory consists of two circles of different radii for $\theta_0 = 0$ and $\pi/24$, corresponding to the multiple periodically flapping states. At $Re = 90$, the phase trajectory starts from the origin for $\theta_0 = 0$, and is trapped in an intermediate radius for a while, and finally converges to a circle identical to that for $\theta_0 = \pi/24$. The intermediate state can be seen from the dense part of the trajectory, which has the same radius as the stable state at $Re = 70$. As the Reynolds number is further increased to 120, the phase trajectory moves smoothly towards the final stable state, which is the same for both $\theta_0 = 0$ and $\pi/24$.

4. Conclusions

The flapping of a flexible ring in a uniform flow was simulated by using an improved version of the immersed boundary method combined with the penalty method to ensure the conservation of the interior ring volume. Both the tension

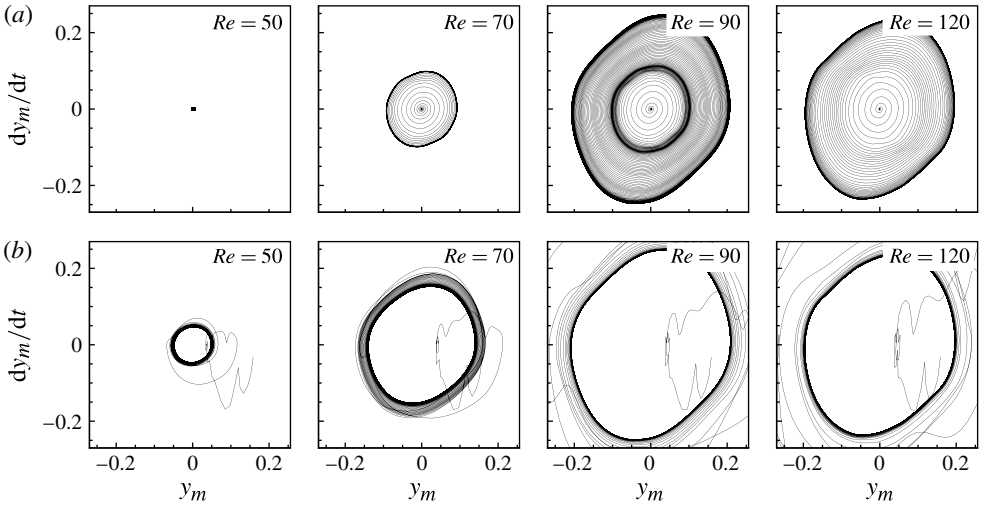

FIGURE 19. Phase maps of the mid-point of a flexible ring of $a/b = 0.67$ at four different Reynolds numbers: (*a*) $\theta_0 = 0$; and (*b*) $\theta_0 = \pi/24$.

and bending forces were considered in the formulation of the ring motion equation. Validation of the proposed method was performed by simulating the flow over a rigid circular cylinder and a freely vibrating ring in an ambient quiescent flow. It was interesting to see that different formulations of the tension force between our work and that of Shoele & Zhu (2010) caused various differences in the results of the fluid–ring coupling system, while our inclusion of the bending rigidity made it possible for us to consider different initial reference shapes rather than the circular one. For an initially circular flexible ring immersed in a uniform flow, different flapping modes were observed by varying the tension or bending coefficients of the ring, which are termed the 'ordinary mode' and the 'energetic mode' in the present study. It was shown that the mode transition leads to abrupt changes in the drag coefficient, lift coefficient, Strouhal number, perimeter and deformation of the ring. From the frequency spectra we saw that the first harmonic is dominant for the energetic mode while the second harmonic is dominant for the ordinary mode, which correspond to the transverse flapping motion and the elastic vibration of the ring respectively. It was also found that the phase difference between the maximum lift coefficient and the maximum transverse position of the mid-point of the ring has a jump due to the transition of flapping modes. Visualization of the vorticity field showed that the ordinary mode corresponds to the classical 2S mode of vortex shedding, while the energetic mode of flapping produces the 2P-like pattern in the near wake. Moreover, for sufficiently small k or γ, the flapping motion also displays some differences, resulting in significant changes in the drag and lift coefficients. For small k the ring motion remains the ordinary mode, while for small γ the flapping persists in the energetic mode. When either k or γ is fixed, the optimal tension and bending coefficients that minimize the drag force on the ring can be obtained before the mode transition. An overall optimal value was found at $k = 9$ and $\gamma = 0.015$ for $Re = 100$ in the present simulations. The effect of the aspect ratio of the ring was then studied. It was shown that the drag coefficient generally decreases as a/b decreases and the mode transition does not occur for $a/b \leqslant 0.5$. However, the drag coefficient is insensitive to a/b once the

energetic mode is formed at large a/b. In our simulations we observed the hysteresis property of the flexible ring, which exhibits bistable states over a range of Reynolds number depending on the initial inclination angle, i.e. one stationary and the other periodically flapping. The variations with aspect ratio in the Reynolds number range of the hysteresis region and the flapping amplitude were investigated. We found that, as the aspect ratio increases, the Reynolds number at which the hysteresis region commences increases and the flapping amplitude of the periodically flapping state decreases. Both trends reach their maximum or minimum values for $a/b = 0.50$. Apart from ordinary bistable states, we also observed another bistability phenomenon, i.e. the presence of two periodically flapping states with different amplitudes depending on the initial inclination angle. The phase relation between the transverse position and the velocity of the mid-point of the ring was examined to further investigate the hysteresis property.

Acknowledgement

This study was supported by the Creative Research Initiatives (No. 2012-000246) programme of the National Research Foundation of Korea.

REFERENCES

ALBEN, S. & SHELLEY, M. J. 2008 Flapping states of a flag in an inviscid fluid: bistability and the transition to chaos. *Phys. Rev. Lett.* **100**, 074301.

BAILEY, H. 2000 Motion of a hanging chain after the free end is given an initial velocity. *Am. J. Phys.* **68**, 764–767.

BELMONTE, A., SHELLEY, M. J., ELDAKAR, S. T. & WIGGINS, C. H. 2001 Dynamic patterns and self-knotting of a driven hanging chain. *Phys. Rev. Lett.* **87**, 114301.

CONNELL, B. S. H. & YUE, D. K. P. 2007 Flapping dynamics of a flag in a uniform stream. *J. Fluid Mech.* **581**, 33–67.

CORTEZ, R. & MINION, M. 2000 The blob projection method for immersed boundary problems. *J. Comput. Phys.* **161**, 428–453.

CORTEZ, R., PESKIN, C. S., STOCKIE, J. M. & VARELA, D. 2004 Parametric resonance in immersed elastic boundaries. *SIAM J. Appl. Maths* **65**, 494–520.

ELOY, C., LAGRANGE, R., SOUILLIEZ, C. & SCHOUVEILER, L. 2008 Aeroelastic instability of cantilevered flexible plates in uniform flow. *J. Fluid Mech.* **611**, 97–106.

FARNELL, D. J. J., DAVID, T. & BARTON, D. C. 2004 Numerical simulations of a filament in a flowing soap film. *Intl J. Numer. Meth. Fluids* **44**, 313–330.

FISH, F. E. & LAUDER, G. V. 2006 Passive and active flow control by swimming fishes and mammals. *Annu. Rev. Fluid Mech.* **38**, 193–224.

GLOWINSKI, R., PANA, T.-W., HESLA, T. I. & JOSEPH, D. D. 1999 A distributed Lagrange multiplier/fictitious domain method for particulate flows. *Intl J. Multiphase Flow* **25**, 755–794.

GOLDSTEIN, D., HANDLER, R. & SIROVICH, L. 1993 Modeling a no-slip flow boundary with an external force field. *J. Comput. Phys* **105**, 354–366.

HUANG, W.-X., SHIN, S. J. & SUNG, H. J. 2007 Simulation of flexible filaments in a uniform flow by the immersed boundary method. *J. Comput. Phys.* **226**, 2206–2228.

HUBER, G. 2000 Swimming in flat sea. *Nature* **408**, 777–778.

JUNG, S., MARECK, K., SHELLEY, M. & ZHANG, J. 2006 Dynamics of a deformable body in a fast flowing soap film. *Phys. Rev. Lett.* **97**, 134502.

KIM, K., BAEK, S.-J. & SUNG, H. J. 2002 An implicit velocity decoupling procedure for the incompressible Navier–Stokes equations. *Intl J. Numer. Meth. Fluids* **38**, 125–138.

KIM, Y. & PESKIN, C. S. 2007 Penalty immersed boundary method for an elastic boundary with mass. *Phys. Fluids* **19**, 053103.

LANDAU, L. D. & LIFSHITZ, E. M. 1987 *Fluid Mechanics*, 2nd edn. *Course of Theoretical Physics*, vol. 6. Butterworth-Heinemann.

LI, Z. & LAI, M.-C. 2001 The immersed interface method for the Navier–Stokes equations with singular forces. *J. Comput. Phys.* **171**, 822–842.

LIAO, J. C., BEAL, D. N., LAUDER, G. V. & TRIANTAFYLLOU, M. S. 2003 Fish exploiting vortices decrease muscle activity. *Science* **302**, 1566–1569.

MÜLLER, U. K. 2003 Fish 'n flag. *Science* **302**, 1511–1512.

PENG, Z., ASARO, R. J. & ZHU, Q. 2010 Multiscale simulation of erythrocyte membrane. *Phys. Rev.* E **81**, 031904.

PESKIN, C. S. 2002 The immersed boundary method. *Acta Numerica* **11**, 479–517.

PESKIN, C. S. & PRINTZ, B. F. 2002 Improved volume conservation in the computation of flows with immersed elastic boundaries. *J. Comput. Phys.* **105**, 33–46.

QI, D. 2007 A new method for direct simulations of flexible filament suspensions in non-zero Reynolds number flows. *Intl J. Numer. Meth. Fluids* **54**, 103–118.

SHIN, S. J., HUANG, W.-X. & SUNG, H. J. 2008 Assessment of regularized delta functions and feedback forcing schemes for an immersed boundary method. *Intl J. Numer. Meth. Fluids* **58**, 263–286.

SHELLEY, M. J., VANDENBERGHE, N. & ZHANG, J. 2005 Heavy flags undergo spontaneous oscillations in flowing water. *Phys. Rev. Lett.* **94**, 094302.

SHOELE, K. & ZHU, Q. 2010 Flow-induced vibrations of a deformable ring. *J. Fluid Mech.* **650**, 343–362.

THESS, A., ZIKANOV, O. & NEPOMNYASHCHY, A. 1999 Finite-time singularity in the vortex dynamics of a string. *Phys. Rev.* E **59**, 3637–3640.

TORNBERG, A.-K. & SHELLEY, M. J. 2004 Simulating the dynamics and interactions of flexible fibres in Stokes flows. *J. Comput. Phys.* **196**, 8–40.

UHLMANN, M. 2006 An immersed boundary method with direct forcing for the simulation of particulate flows. *J. Comput. Phys.* **209**, 448–476.

WILLIAMSON, C. H. K. & ROSHKO, A. 1988 Vortex formation in the wake of an oscillating cylinder. *J. Fluids Struct.* **2**, 355–381.

YU, Z. 2005 A DLM/FD method for fluid/flexible-body interactions. *J. Comput. Phys.* **207**, 1–27.

ZHANG, J., CHILDRESS, S., LIBCHABER, A. & SHELLEY, M. 2000 Flexible filaments in a flowing soap film as a model for one-dimensional flags in a two-dimensional wind. *Nature* **408**, 835–839.

ZHANG, L. J & ELDREDGE, J. D. 2009 A viscous vortex particle method for deforming bodies with application to biolocomotion. *Intl J. Numer. Meth. Fluids* **59**, 1299–1320.

ZHU, L. & PESKIN, C. S. 2002 Simulation of a flapping flexible filament in a flowing soap film by the immersed boundary method. *J. Comput. Phys.* **179**, 452–468.

ZHU, L. & PESKIN, C. S. 2003 Interaction of two flapping filaments in a flowing soap film. *Phys. Fluids* **15**, 1954–1960.